# PCCP

Accepted Manuscript

ROYAL SOCIETY OF CHEMISTRY

www.rsc.org/pccp

# Strain induced crystallization and melting of natural rubber during dynamic cycles

*Nicolas Candau* [a,b], *Laurent Chazeau* *[a,b], *Jean-Marc Chenal* [a,b], *Catherine Gauthier* [c], *José Ferreira* [a,b], *Etienne Munch* [c], *Dominique Thiaudière* [d]

[a] Université de Lyon, CNRS

[b] MATEIS, INSA-Lyon, CNRS UMR5510, F-69621, France

[c] Manufacture Française des Pneumatiques Michelin, Centre de technologies, 63040 Clermont Ferrand Cedex 9, France

[d] Synchrotron SOLEIL - Ligne de lumière DIFFABS, L'orme des merisiers, Saint Aubin, 91192 Gif sur Yvette, France

*Corresponding author: Laurent Chazeau, e-mail: laurent.chazeau@insa-lyon.fr

**Keywords**: strain-induced crystallization, natural rubber, in situ WAXS, self-heating

## Abstract

Strain-induced crystallization (SIC) of natural rubber (NR) is studied during dynamic cycles at high frequency (with equivalent strain rates ranging from 7.2 $s^{-1}$ to 290 $s^{-1}$). Different testing parameters are varied: the frequency, the temperature and the stretching ratio domain. It is found that an increase of the frequency leads to an unexpected form of the CI-λ curve, with a decrease of the crystallinity during both loading and unloading steps of the cycle. Nevertheless, the interpretation of the curves needs to take into account several phenomena such as (i) an instability of the crystallites generated during the loading step, which increases with the frequency, (ii) the memory of the previous alignment of the chains, which depends on the minimum stretching ratio of the cycle $\lambda_{\min}$ and of the frequency, (iii) self-heating which makes

more difficult the crystallites nucleation and easier their melting. Thus, when the stretching ratio domain is above the expected stretching ratio at complete melting $\lambda_{melt}$, the combination of these phenomena leads, at high frequency, to unexpected results such as a complete melting at $\lambda_{min}$, and to an hysteresis in the CI-$\lambda$ curves.

## 1. Introduction

The excellent mechanical properties of natural rubber (NR) are thought to be the consequence of its ability to crystallize under strain. In particular, there are ongoing works to understand the fracture [1, 2], crack growth [3-7] and fatigue behaviour [8, 9] of NR and their relationship with strain induced crystallization (SIC). This phenomenon was for the first time evidenced by Acken and Long [10, 11] only few years after the discovery of SIC in 1925 [12]. These pioneering works evidenced that SIC is a kinetic phenomenon which requires a very short time (less than one second) to occur when the rubber is stretched at a sufficiently high stretching ratio. For that reason, SIC kinetics remains difficult to characterize.

In literature, the strategy to study it has often been indirect, by the use of thermal [13-15] or mechanical measurements [16]. Unfortunately, these techniques provide only partial information, as they do not give access to the crystalline microstructure. The progressing ability of X-rays detectors has then been used to capture more and more rapidly a diffraction pattern. In particular, recent in situ WAXS experiments using impact tensile test [17, 18] allowed evaluating SIC process on a sample rapidly stretched and relaxed in the deformed state. These papers give interesting results concerning the kinetics of the incipient crystallites in the deformed state, but they do not allow performing measurement during the deformation of the sample.

The stroboscopic approach can be used to solve this problem. It allows recording WAXS patterns by accumulation of the diffracted intensity thanks to a stroboscopic acquisition. The advantages of such a technique are first to avoid any averaging over an elongation domain (since a stroboscopic device selects the desired elongation level), secondly to enable in situ WAXS measurements in a frequency range never reached before. With this technique, Kawai et al. [19] clearly evidenced that the crystallinity of a vulcanized natural rubber, measured during the dynamic cycles, decreases when frequency increases from 0.1 Hz to 10 Hz. More recently, Albouy et al. [20] used the same approach but in a larger frequency range (from 0.01 Hz to 50 Hz) and studied both crystallization and melting kinetics whose characteristic times were found around several decades of milliseconds. We also published preliminary results showing how SIC kinetics accelerates with the stretching ratio [21]. However, these studies only focused on the SIC characteristics at the minimum and at the maximum stretching ratio reached during the dynamic cycle, and not on its evolutions in between these two values.

Thus, the present paper is dedicated to the study of SIC during a complete dynamic cycle at high frequencies thanks to the improvement of our stroboscopic device. The experimental procedure allows to completely follow both crystallization and melting processes of NR samples when stretched in conditions of solicitation similar to those met in usual applications (for instance in damping applications). A complete analysis of the crystalline features such as the crystallinity index (CI), the crystallites sizes ($L_{hkl}$), their orientation ($\psi_{hkl}$) is developed. Several loading and thermal conditions are explored thanks to various pre-stretching conditions and temperatures. This last parameter is known to be a major one that controls SIC in NR at “slow” strain rate [22, 23, 16]. Its effect on SIC during cycles at high stretching ratios and strain rates is especially discussed in the last section.

## 2. Materials and experiments

### *2.1. Materials*

The samples composition is the following: NR rubber gum (Technically Specified Rubber TSR20) provided by Michelin Tire Company, stearic acid (2 phr, i.e. 2 g per 100 g of rubber), ZnO (1.5 phr), 6PPD (3 phr), CBS (1.9 phr) and sulfur (1.2 phr). The material has been processed following the Rauline patent [24]. First, the gum is introduced in an internal mixer and sheared for 2 min at 60°C. Then, the vulcanization recipe is added and the mix is sheared for 5 min. The material is afterward sheared in an open mill for five minutes at 60°C. Sample sheets are then obtained by hot pressing at 170°C during 13 min. Dumbbell-shaped samples, with a 6 mm gauge length ($l_0$) and 0.8 mm thickness, are machined. The average network chain density $\nu$ was estimated from the swelling ratio in toluene and from the Flory – Rehner equation [25] and found equal to $1.4 \times 10^{-4}$ mol.cm$^{-3}$. This density is tuned so that (i) it promotes the development of strain-induced crystallization [26] and (ii) it is high enough to avoid an inverse yield effect [27]. In order to avoid microstructure modification during the different mechanical tests, i.e. an uncontrolled Mullins effect, the samples are stretched four times up to stretching ratio ($\lambda$ = 7) higher than the maximum stretching ratio reached during the in situ cyclic tests ($\lambda$ = 6).

### *2.2. In situ WAXS measurements at slow strain rate*

The in situ WAXS experiments are carried out on the D2AM beamline of the European Synchrotron Radiation Facility (ESRF). The X-ray wavelength is 1.54 Å. Tests consist of stretching a NR sample at a constant strain rate ($4.2 \times 10^{-3}$ $s^{-1}$) and at fixed temperature.

The two-dimensional (2D) WAXS patterns are recorded by a CCD camera (Princeton Instrument). The background, (i.e. air scattering and direct beam intensities) is properly measured in absence of any sample. It can then be subtracted to the total intensity scattered in the presence of the rubber sample. The corrected scattering intensity is finally normalized by the thickness and the absorption of the sample. Each scattering pattern is integrated azimuthally (0° up to 180°) when crystal reflection appears. The deconvolution of the curve $I=f(2\theta)$ enables the extraction of the intensity at the peak top and the width at half height of each crystalline peak and the intensity at the peak top of the amorphous phase. The crystallinity index CI is then determined as follows [28]:

$$CI = \frac{I_{a0} - I_{a\lambda}}{I_{a0}} \tag{1}$$

where $I_{a0}$ and $I_{a\lambda}$ are the intensity of the amorphous phase at the peak top in the unstretched state and the stretched state, respectively. The average crystallite sizes $L_{hkl}$ ($L_{200}$, $L_{102}$ and $L_{002}$) in the direction normal to the (*hkl*) planes, are estimated from the Scherrer equation:

$$L_{hkl} = \frac{K\lambda_w}{\beta_{1/2} cos\theta} \tag{2}$$

where $\lambda_w$ is the wavelength and θ is the Bragg angle. In this study, each crystalline peak is fitted with a Lorentzian function in which the width at half-height is $\beta_{1/2}$. According to the parameters chosen for the fit of the experimental peak, the K value is 0.64 [29]. In order to measure the average crystallite size in the stretching direction $L_{002}$ ($c_1$), the tensile test machine is tilted by an angle around 10°.

The orientation of crystallites $\psi_{\mathrm{hkl}}$ is given by half width at half-height of the crystalline peak in the direction normal to the plane (hkl), integrated over the azimuth.

### *2.3. In situ WAXS measurements in dynamic conditions*

The in situ WAXS measurements during dynamic cycles are carried out on the Diffabs beamline of the French national Synchrotron SOLEIL. A specifically dedicated apparatus was developed in order to perform WAXS measurements during high velocity cyclic tensile tests with large amplitude and high frequencies (up to 80 Hz) [21] (figure 1). Thanks to a stroboscopic acquisition, the diffraction pattern is not averaged over the whole cycle, but is acquired at a chosen stretching ratio. In addition, the temperature increase of the material, which can be significant at high frequencies and large amplitude, is also estimated during the test thanks to the measurement of the sample surface temperature with an Infra-Red pyrometer (CTLF-CF3-C3) of Microepsilon.

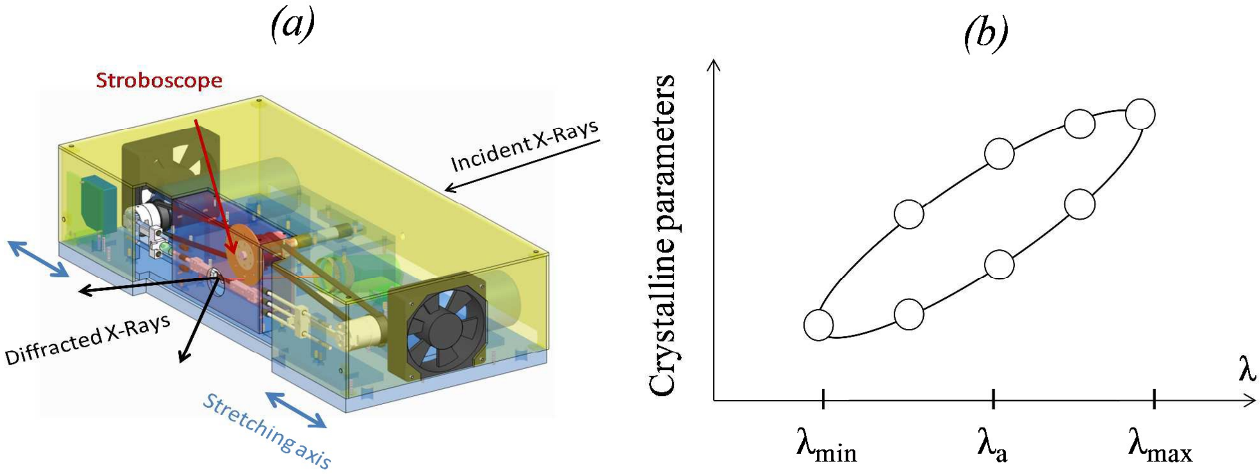

Figure 1. (a) View of the homemade machine. (b) Reconstruction of the “crystallinity cycle”.

The stroboscopic acquisition of the WAXS pattern at the chosen stretching ratio is made so that the time of exposure is 1/44th of the time for a complete cycle. This means that a 1 sec exposure time at given elongation needs an acquisition over 44 cycles. The device enables to dynamically stretch the samples over a fixed amplitude $\Delta\lambda = \lambda_{max}-\lambda_{min}$ ranging from 0 to 2, around an average stretching ratio $\lambda_a$ fixed at the beginning of the experiment. The testing procedure is the following: the NR sample is first rapidly pre-stretched at $\lambda_a$ and let to relax in the deformed state during five minutes. Sample is then dynamically deformed around $\lambda_a$ with the total amplitude $\Delta\lambda$

with an increasing frequency (from 2Hz to 80Hz). Once this sequence is finished, the sample is kept at $\lambda_a$ during five minutes. During this relaxation phase, the aperture of the stroboscopic system is changed for another position. This procedure is repeated for 8 positions of the cycle, allowing measuring the crystalline parameters during the whole cycle (figure 1). In order to limit fatigue during the dynamic tests, each sample is submitted to only four dynamic sequences (four positions), i.e. two samples are used to describe the whole cycle.

Tests called hereafter A, B and C, are performed at room temperature, whereas tests E and F are performed at 50°C. Pre-stretching values $\lambda_a$ are modified in order to perform cyclic tests above or below the melting stretching ratio $\lambda_{melt}$. This melting stretching ratio corresponds to the stretching ratio of complete melting of crystallites during unloading of a cyclic test performed at slow strain rate ($4.2 \times 10^{-3}$ $s^{-1}$) and at a given temperature. The dynamic amplitude $\Delta\lambda$ is chosen equal to 1.8. This value is high enough to expect a significant variation of CI during the dynamic cycle. Indeed, if the amplitude is too low, the CI variations measured during the cycle are too weak (unpresented data).

## 3. Results

### 3.1. Influence of the stretching ratio domain

We first study the effect of the stretching ratio domain explored during dynamic cycles performed at room temperature and at 2 Hz (figure 2a). The cycle of a NR sample stretched at room temperature and at slow strain rate ($4.2 \times 10^{-3}$ $s^{-1}$ equivalent to $10^{-3}$ Hz), so called hereafter “the reference curve” is added on the same figure. The loading conditions of these tests are given in figure 2a. Figure 2b presents the evolution of CI as a function of the stretching ratio domain. For the slow strain rate cycle (test D), the first crystallites appear during the loading step at $\lambda_{cryst}$ = 4.3, so-called hereafter stretching ratio at SIC onset. During unloading, CI progressively decreases and the crystalline phase totally disappears at the melting stretching ratio $\lambda_{melt}$ = 3. Concerning the dynamic tests, two cases can be distinguished: the cycle can be performed partly or totally above the melting stretching ratio $\lambda_{melt}$ corresponding to the conditions $\lambda_{min} \leq \lambda_{melt}$ or $\lambda_{min} > \lambda_{melt}$ respectively. For dynamic tests A and B, SIC is poorly developed during the cycle and no hysteretic shape is observed. This is due to (i) a low $\lambda_{max}$ value which avoids a strong increase of CI during loading and (ii) a low $\lambda_{min}$ value which is below or equal to $\lambda_m$ and thus leads to the complete melting of crystallites during unloading. For test C, CI is strongly enhanced not only due to an increase of $\lambda_{max}$ but also to the value of $\lambda_{min}$, which is now above $\lambda_{melt}$, avoiding the complete melting during unloading. In spite of a stretching ratio domain above $\lambda_{melt}$, a crystalline hysteresis is still observed. This is therefore different from what was observed during cyclic experiments at slow strain rate: Candau et al. [30] evidenced that, even after their melting, the chains of the crystallites keep the memory of their alignment, as far as the stretching ratio has not been decreased down to $\lambda_{melt}$. This eases crystallite nucleation during reloading, leading to the disappearance of the crystallinity hysteresis.

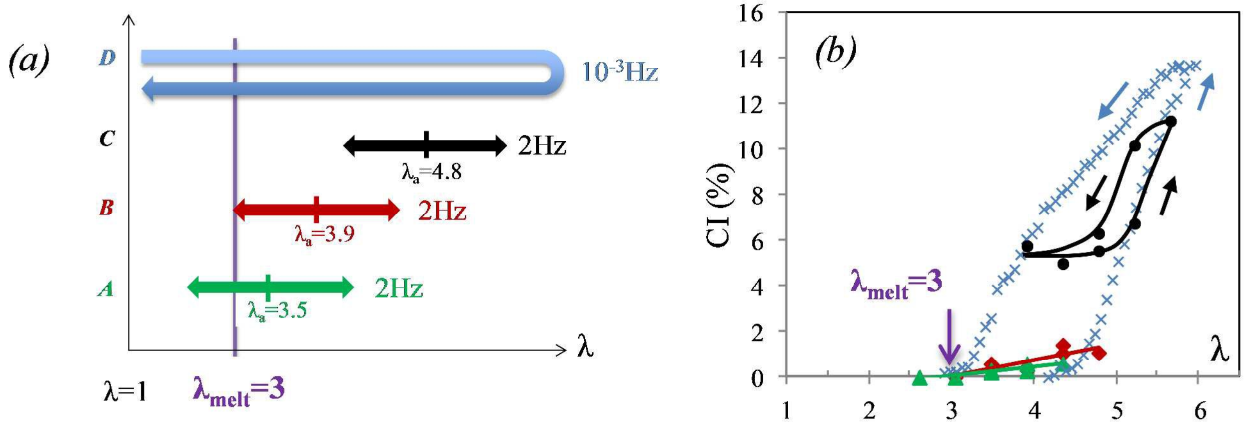

Figure 2. (a) Loading conditions of tests: A ($\lambda_a$=3.5), B ($\lambda_a$=3.9), C ($\lambda_a$=4.8) and D. (b) CI versus $\lambda$ during the cycles: test A (triangle symbols), test B (diamond symbols), test C (circle symbols) and test D (cross symbols).

### *3.2. Influence of the frequency*

The frequency of the dynamic cycles is now increased up to several decades. The temperature of the testing chamber is fixed at 21°C. For tests performed with $\lambda_{min} \leq \lambda_{melt}$, CI continuously decreases with the increase of the frequency (unpresented data). For the test performed above $\lambda_{melt}$ (figure 3), when the frequency increases from 2 Hz to 5 Hz, the CI curve seems shifted to a lower value but its hysteretic shape is unchanged. At 10 Hz, CI suddenly falls. From 10 Hz to 40 Hz, CI continues to decrease and reaches zero at $\lambda_{min}$. The hysteretic shape is no more visible because of the low CI values measured. The CI cycles are then very similar to those observed during the tests performed with $\lambda_{min} \leq \lambda_{melt}$ in spite of the fact that the stretching ratio domain should be *a priori* always above $\lambda_{melt}$. Thus, the increase of the frequency might be equivalent to an increase of $\lambda_{melt}$, the stretching ratio at complete melting. This will be further discussed in relation with the observed increase of the sample temperature with the frequency.

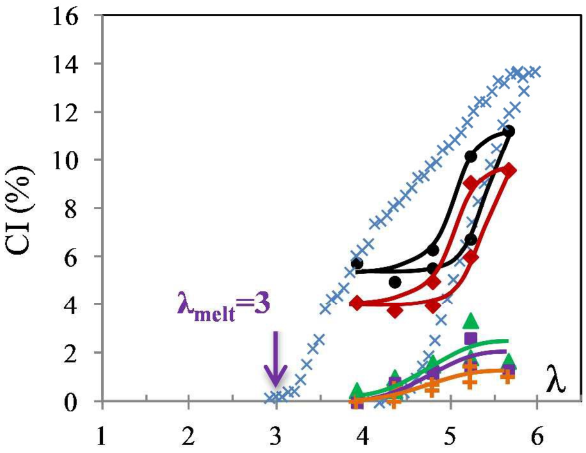

Figure 3. CI versus $\lambda$ during test C performed at room temperature at 2 Hz (circle symbols), 5 Hz (diamond symbols), 10 Hz (triangle symbols), 20 Hz (square symbols) and 40 Hz (plus symbols). The slow strain rate cycle is added for comparison (cross symbols).

### *3.3. Influence of the ambient temperature*

Whereas the previous tests were performed at room temperature, dynamic tests are now performed in a chamber whose temperature is fixed at 50°C (figure 4). Two cases are studied, one where $\lambda_{min} \leq \lambda_{melt\ (50°C)}$ and another where $\lambda_{min} > \lambda_{melt\ (50°C)}$ (tests E and F respectively), where $\lambda_{melt\ (50°C)}$ is now the melting stretching ratio of complete melting measured at slow strain rate and 50°C. As for the tests at room temperature: (i) for the lowest frequency, all crystallites melt during unloading in the case of the test E but not for the test F, (ii) when the frequency increases, CI decreases whatever the stretching ratio and CI at $\lambda_{min}$ finally decreases down to zero, even for the test initially performed above $\lambda_{melt(50°C)}$.

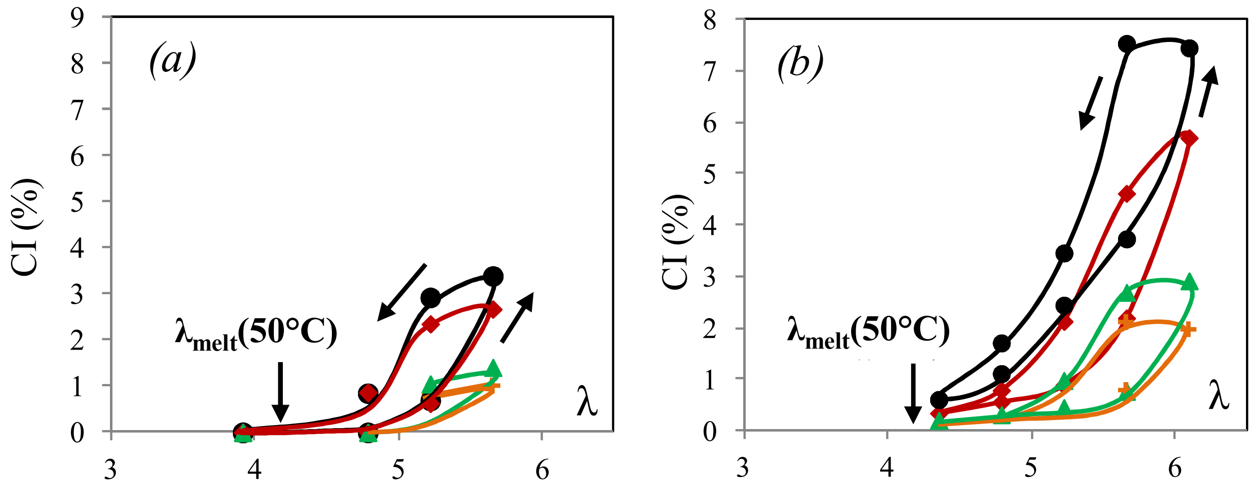

Figure 4. CI versus $\lambda$ during dynamic tests: E (a) and F (b) performed at 2 Hz (circle symbols), 5 Hz (diamond symbols), 10 Hz (triangle symbols), and 40 Hz (plus symbols). Arrows indicate the direction of the cycles.

## 4. Discussion

The different results are complex to interpret as they depend on several interdependent parameters: temperature, frequency, and $\lambda_{melt}$. Moreover, as discussed below, different phenomenon involved in the strain-induced crystallization during dynamic cycles must be taken into account.

### *4.1. Strain rate and memory effects on crystallization*

The hysteretic shape of the CI curve observed during the cyclic deformation at slow strain rate (test D, figure 2) is explained by the kinetic nature of the crystallization process which needs time to occur, whereas melting can be considered as instantaneous and the CI melting curves as representative of the thermodynamic equilibrium. Thus, due to the kinetics aspect of SIC, crystallization should depend on strain rate. This was evidenced by monotonic tests performed with strain rates varying from $4.2 \times 10^{-3}$ s$^{-1}$ (same strain rate than the reference cycle) to $2.8 \times 10^{1}$ s$^{-1}$ (close to the equivalent strain rate in the test C, at 2 Hz) which show that the stretching ratio at SIC onset ($\lambda_c$) is delayed from 4.3 to 5.3 [31]. With the sole knowledge of the crystallization during a simple loading in tensile test, we would have expected for the loading curve at 2Hz, a crystallization onset at higher $\lambda_c$ and therefore a lower CI at a given $\lambda$. In a previous paper [30], successive cycles have been performed at slow strain rate, with an increasing minimum stretching ratio $\lambda_{min}$ ($\lambda_{min}$ is below $\lambda_{melt}$ for the first cycle and above for the following ones). The second loading curve (and also the following ones), was found to be drastically shifted to lower stretching ratios compared to the first loading crystallization curve, and actually was found quite close to the first unloading melting curve. The experimental results of references 30 and 35 showed that during a mechanical cycle (between $\lambda_{min}$ and $\lambda_{max}$) performed at slow strain rate ($10^{-3}s^{-1}$), the crystallinity index increase is the result of a progressive increase (decrease) of the number of crystallites during loading (unloading). As we proposed in ref 30, it also suggests that these crystallites from several populations which successively nucleate at different stretching ratios belonging to the ($\lambda_c$; $\lambda_{max}$) domain, and successively melt in the reverse order between $\lambda_{max}$ and $\lambda_{melt}$. For instance, the most stable population nucleates at $\lambda_c$ and melts at $\lambda_{melt}$, while the less stable population crystallizes at $\lambda_{max}$ and melts instantaneously during unloading. Moreover, for slow strain rates like those used in ref. 30, the growth of these populations can be assumed instantaneous once they have nucleated. This interpretation was consistent with SIC performed at different temperature and presented in ref 35.

Thus, within this scenario, still considering that the crystallite growth is instantaneous, when a cycle is performed above $\lambda_{melt}$, during unloading, the involved crystallite populations can melt between $\lambda_{max}$ and $\lambda_{min}$ and then recrystallize during reloading, while the populations which melt between $\lambda_{min}$ and $\lambda_{melt}$ remain thermally stable (if the temperature of the test in unchanged). The fact that at slow strain rate, for cyclic test above $\lambda_{melt}$, the crystallinity hysteresis is much smaller than during a cyclic test with $\lambda_{min} < \lambda_{melt}$, and that the CI reloading curve is actually close to the CI unloading curve (in other word, during reloading, the re-nucleation of the crystallites which have melted during unloading is easier), was ascribed to a “memory effect”: the chains of the crystallites which have molten during unloading keep the memory of their previous alignment, this facilitates the crystallites re-nucleation during the following loading step.

Actually, one might also use the concept of a secondary nucleation, i.e. a nucleation which occurs more easily because of the presence of existing crystallites. Nevertheless, given the limited size of the existing crystallites, which, to our opinion rapidly reach their saturated size because of the crosslinks presence, and given the stress relaxation that occurs in the amorphous phase in the crystallite vicinity (as described and modeled by Flory), we think unlikely the formation of crystallites from the surface of the existing ones (as often observed in classical thermal crystallization). Thus, if a secondary nucleation effect should be proposed to explain the reloading CI-λ curve, it must be understood as the fact that the nucleation of new crystallites during reloading is eased by the complex strain/stress field in the elastomer resulting from the existing crystallites.

To sum up, the crystallinity developed during the loading step of the dynamic cycle performed at 2Hz and above $\lambda_{\text{melt}}$ probably results from a combined effect of the high strain rate which should decrease CI at a given stretching ratio, and of this memory effect (or secondary nucleation effect), which, conversely, increases CI, as illustrated in figure 5.

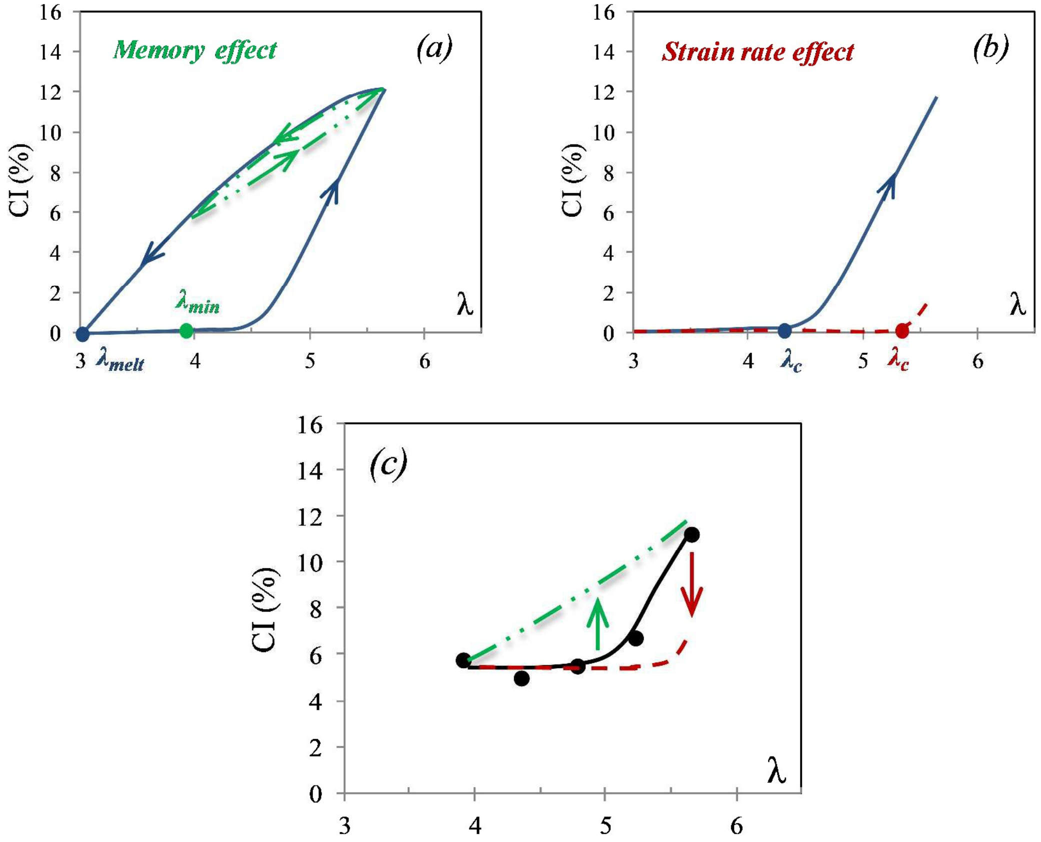

Figure 5. (a) Schematic evolution of CI versus λ for a slow strain rate cycle performed with $\lambda_{\text{min}} < \lambda_{\text{melt}}$ (solid line) and for a slow strain rate cycle performed with $\lambda_{\text{min}} > \lambda_{\text{melt}}$ (double dotted line). (b) Schematic evolution of CI versus λ for a monotonic loading at slow strain rate (solid line) and at high strain rate (dotted line). (c) Crystallization curve obtained during the loading step of test C performed at 2 Hz (data points and solid line). Schematic evolution of the crystallization

curve of a slow strain rate cycle performed above $\lambda_{melt}$ (double dotted line), and during a loading at high strain rate (dotted line).

*4.2. Melting acceleration*

The fact that the CI value measured at $\lambda_{min}$ is the same at slow strain rate (during the unloading step) and at 2Hz (cf. figure 3) is consistent with the scenario that each crystallite population involved in the dynamic cycle nucleates during the loading and completely melts during unloading. In other words, the measured CI at $\lambda_{min}$ results from the summation of thermally stable crystallites (figure 6) which are not involved in the dynamic cycle and thus do not disappear as long as the temperature of the test is maintained constant. However, as commented previously, the shape of the CI curve during unloading of test C at 2 Hz (figure 2) is different from that of the unloading curve of test D (slow strain rate): the crystallites population involved in the cyclic crystallization melt more easily, i.e. at higher stretching ratio when the cycle is performed at high strain rate. This indicates a weaker thermal stability of these crystallites compared to those formed at slow strain rate (cf. figure 6). Same phenomenon was also observed on our filled NR samples [32] stretched in similar loading conditions.

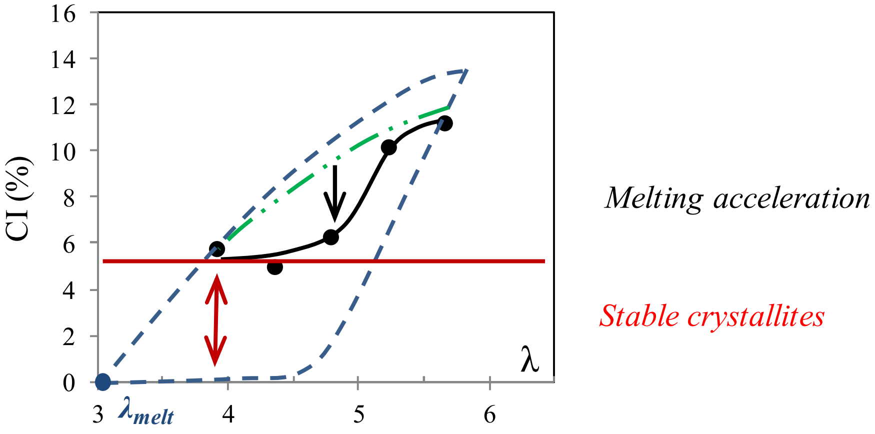

Figure 6. CI versus $\lambda$ during the unloading step of test C performed at 2 Hz (data points and solid line). Shape of the reference curve (dotted line). Shape of the unloading of a cycle performed above $\lambda_{melt}$ and with the same $\lambda_{max}$ than that of test C (double dotted line). Single arrow indicates the melting acceleration during unloading of test C and double arrow the CI at $\lambda_{min}$ resulting from the accumulation of thermally stable crystallites.

The measurement of the crystallite dimensions and orientation could provide additional information on their stability. Figure 7a shows the orientation of the crystallites as a function of the stretching ratio for test C. The crystallites orient during the loading and slightly disorient during unloading, which is consistent with tests performed at slow strain rate [26, 33]. At a given stretching ratio, crystallites are slightly less oriented during unloading compared to loading, leading to a weak hysteresis. An increase of the frequency does not change the values of crystallite orientation: therefore, the orientation of the crystallites is only strain and not strain rate dependent.

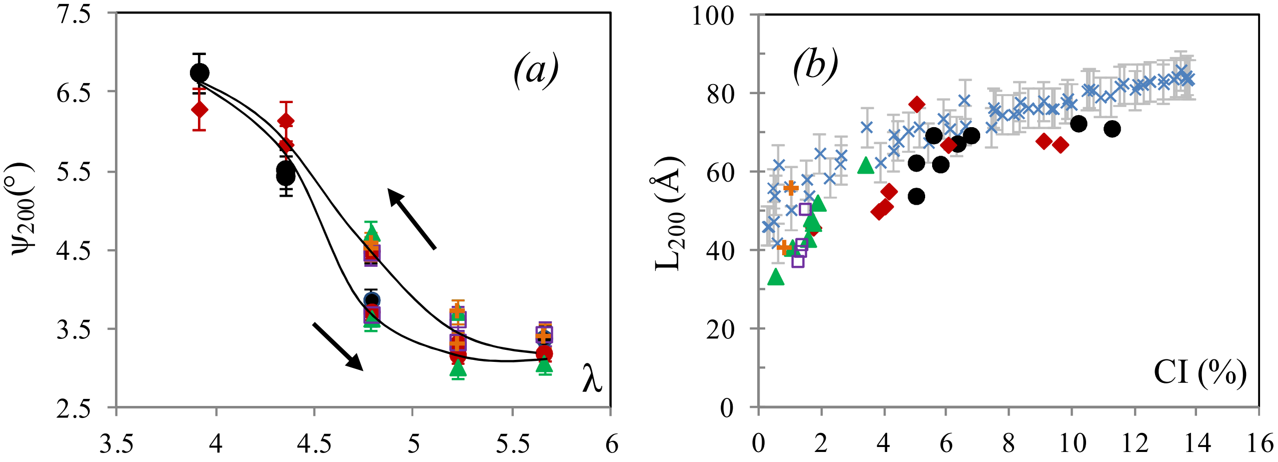

Figure 7. (a) Orientation of crystallites versus $\lambda$ for test C performed at 2 Hz (circle symbols), 5 Hz (diamond symbols), 10 Hz (triangle symbols), 20 Hz (square symbols) and 40 Hz (plus symbols). (b) Corresponding $L_{200}$ - CI curves. Arrows indicate the direction of the cycle. Lines are a guide for the eyes. The $L_{200}$ - CI curve from test D is added (cross symbols).

The crystallite dimensions in the three principal directions (200), (120) and (002) of the orthorhombic structure of NR crystallites have been extensively studied during cyclic loadings at slow strain rates [26, 30, 33, 34]. According to these studies, the ratio between $L_{120}$ and $L_{200}$ is kept constant during loading or unloading phase. Moreover, the $L_{002}$ is found roughly constant with the stretching ratio [26, 30]. The 1/3 ratio relationship between the two principal lateral crystallite sizes ($L_{120}$ and $L_{200}$) was also found during our dynamic tests as well as the invariance with the stretching ratio of the size in the stretching direction (002). Thus, only the evolution of the size $L_{200}$ will be discussed here: figure 7b presents its evolution as a function of CI for the dynamic test C (curves obtained with test A, B, E and F not presented here lead to the same comments).

For comparison, the evolution of $L_{200}$ during the cycle at slow strain rate and room temperature (test D) is also plotted. The L-CI curves found during the dynamic tests are slightly below the one obtained during slow strain rate cycle. In ref. 30, we stated that the crystallite appearance of each population is divided into two steps: polymer chains are first extended to create a nucleus from which folded chains lamella quickly grows. In that study, we also estimated a small volume ratio between nucleus and the corresponding crystallite. Thus, within the frame of the scenario previously recalled, a crystallites growth too slow compared to the cycle duration would have led to a very different shape of the L-CI curve: (i) at low CI, the number of crystallite nuclei would have been accumulated with no significant change in the measured crystallites size and (ii) at high CI, the crystallites size would have strongly increase due to the growth of the previously nucleated crystallite populations. Contrarily, in figure 7b, for a given CI, the average crystallites size is found almost independent on the strain rate (or frequency). This suggests that the order of appearance of the different populations does not change with the strain rate and that their growth can be still considered as instantaneous. Thus, SIC kinetics is still rather controlled by nucleation.

Nevertheless, the slightly lower $L_{200}$ could indirectly indicate that the amorphous phase surrounding the crystallites is not in the same state as in the case of a much slower cyclic solicitation. During the crystallite growth, topological constraints (trapped entanglements and crosslinks) should be rejected from the crystallite and should accumulate in the close vicinity of the crystallite surface. This is the reasonable explanation that can be given to the limited and stabilized size of the crystallites, in addition to the amorphous chain explanation given by Flory. Such accumulation of topological constraints around the crystallites surface should be equivalent to an increase of their interfacial energy [36]. Going further, the easier melting observed at high frequency during unloading might be due to the fact that, when stretched at high frequency, the amorphous chains and the topological constraints (entanglements and chemical crosslinks) surrounding the crystallites do not have the time to be properly relaxed. This should be equivalent to a higher interfacial energy of the crystallites which could thus promote their melting. This would also explain a weaker memory effect and therefore the hysteresis of the CI-$\lambda$ curves. Of course such interpretation would need further experimental evidences which are not in the scope of this study.

### *4.3. Self-heating*

As shown on figures 3 and 4b, CI at $\lambda_{min}$ for the tests performed above $\lambda_{melt}$ (tests C and F) decreases with frequency. The most reasonable explanation is that the temperature of the test increases with frequency, leading to an increase of $\lambda_{melt}$ increases. This is indeed the case, as shown on figure 8a where the surface temperature during test C is plotted as a function of the frequency. This self-heating (equal to $T_{surface} - T_i$, with $T_i$ the ambient external temperature which is here equal to 21°C) is likely due to viscoelastic effects and thus logically increases with frequency.

In order to estimate more precisely the temperature influence on the melting stretching ratio $\lambda_{melt}$, a series of WAXS experiments has been performed at slow strain rate ($4.2 \times 10^{-3}\ s^{-1}$) at different temperatures (diamond in figure 8b) and modeled with a thermodynamic approach (curve in figure 8b) proposed in a previous work [35]. From this evolution, assuming the equivalence between heat brought by self-heating and heat brought by an external source, the effect of self-heating on the melting stretching ratio can be evaluated for any given frequency.

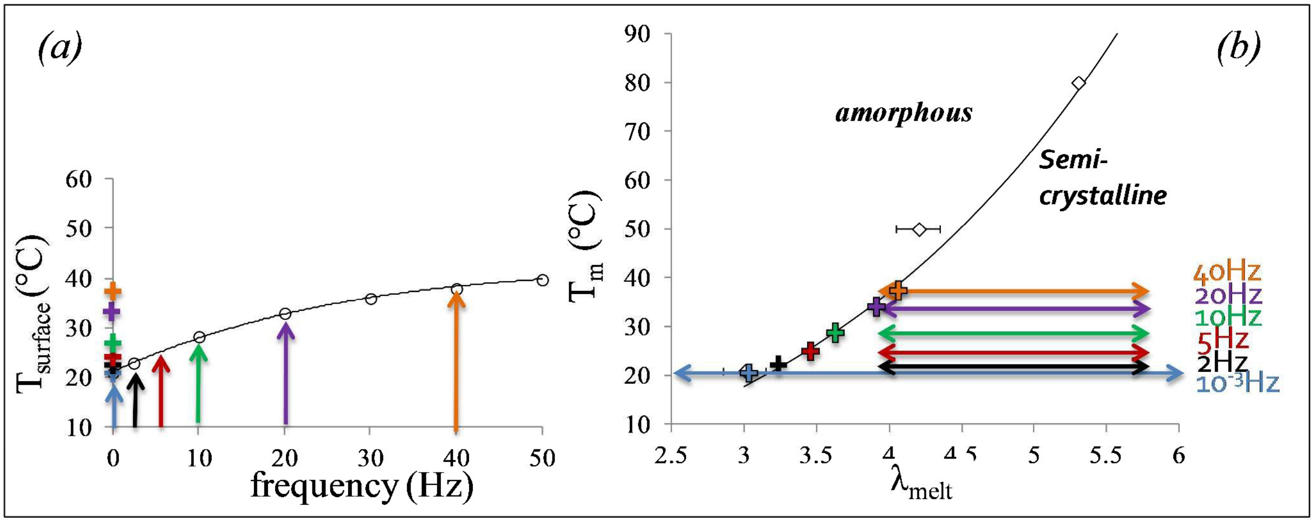

Figure 8. (a) Effect of the frequency on self-heating during test C and (b) relation between the melting temperature and the melting stretching ratio. Loading conditions of test D (double arrows) are added at the temperature corrected from self-heating measured for each frequency.

As shown in figure 3, the crystallinity at $\lambda_{min}$ disappears at 20 Hz. This frequency is precisely the one for which $\lambda_{melt}$ reaches the value $\lambda_{min}$ because of self-heating (figure 8b). Same method has been applied to test F and leads to similar conclusions. Self-heating also decreases significantly the CI developed between $\lambda_{\text{min}}$ and $\lambda_{\text{max}}$ for two reasons: (i) the direct consequence of the increase of $\lambda_{\text{melt}}$ above $\lambda_{\text{min}}$ is a loss of the memory effect and therefore an increase of the nucleation time, (ii) this nucleation time is also directly increased by the temperature increase.

Indeed, as already shown in a large number of studies [16, 22, 23] with tensile tests experiments at slow strain rate the ability of NR to crystallize is weaker when temperature is increased above room temperature. In particular, the stretching ratio at SIC onset $\lambda_{\text{cryst}}$ is increased: the molecules must be more stretched in order to allow a sufficiently rapid nucleation within the time of the experiment. In other words, the strain energy (proportional to $\lambda^2$) must be higher, in order to compensate the larger enthalpic energy of crystallite formation [35].

## 5. Conclusion

A dynamic tensile test machine recently developed was used in order to study strain-induced crystallization (SIC) of natural rubber (NR) during dynamic cycles at high frequency (with equivalent strain rates ranging from 7.2 $s^{-1}$ to 290 $s^{-1}$). Different testing parameters have been studied: the frequency, the ambient temperature and the stretching ratio domain. As expected, in all cases, an increase of the frequency leads to a decrease of the SIC phenomenon during both the loading and the unloading steps. Nevertheless, the interpretation of the curves needed to take into account several phenomenon such as (i) an instability of the crystallites generated during the loading step, which increases with the frequency, (ii) the memory of the previous alignment of the chains, which depends on the minimum stretching ratio of the cycle $\lambda_{\text{min}}$ and of the frequency, (iii) self-heating which makes more difficult the crystallites nucleation and easier their melting. Thus, when the stretching ratio domain is much above $\lambda_{\text{melt}}$, their combination leads at high frequency to unexpected results such as a complete melting at the lowest stretching ratio of the cycle $\lambda_{\text{min}}$, and an unexpected form of the hysteresis in the CI-$\lambda$ curve. Obviously, these experimental data, and the complexity of the SIC that they highlight, strongly suggest that only physical model coupling the mechanics, the thermic and the thermodynamic will be able to provide a pertinent description of this phenomenon [37].

## 6. Acknowledgements

The authors are indebted to the synchrotron SOLEIL and the local contact Dominique Thiaudière for providing the necessary beamline time and technical assistance in the experiments on the DiffABS line.

## 7. References

1. L. González, J. L. Valentín, A. Fernández-Torres, A. Rodriguez and A. Marcos-Fernández, *Journal of Applied Polymer Science.*, 2005, **98**, 1219-1223.
2. P. Y. Le Gac, M. Broudin, G. Roux, J. Verdu, P. Davies and B. Fayolle, *Polymer.*, 2014, **55**, 2535-2542.
3. P. Rublon, B. Huneau, N. Saintier, S. Beurrot, A. Leygue, E. Verron, C. Mocuta, D. Thiaudiere and D. Berghezan, *Journal of Synchrotron Radiation.,* 2013, **20**, 105-109.
4. J. B. Le Cam and E. Toussaint, *Macromolecules.*, 2010, **43**, 4708-4714.
5. S. Trabelsi, P. A. Albouy and J. Rault, *Macromolecules.*, 2002, **35**, 10054-10061.
6. K. Bruning, K. Schneider, S. V. Roth and G. Heinrich, *Macromolecules.,* 2012, **45**, 7914-7919.
7. J. S. Martinez, X. Balandraud, E. Toussaint, J. B. Le Cam and D. Berghezan, *Polymer.*, 2014, **55**, 6345-6353.
8. S. Beurrot-Borgarino, B. Huneau, E. Verron, and P. Rublon, *International Journal of Fatigue.*, 2013, **47**, 1-7.
9. N. Saintier, G. Cailletaud and R. Piques, *Materials Science and Engineering: A.,* 2011, **528**, 1078-1086.

10 J. D. Long, W. E. Singer and W. P. Davey, *Industrial & Engineering Chemistry.*, 1934, **26**, 543-547.

11 M. F. Acken, W. E Singer and W. Davey, *Industrial & Engineering Chemistry.*, 1932, **24**, 54-57.

12. J. R. Katz, *Naturwissenschaften*., 1925, **13**, 410-416.

13. J. R. S. Martinez, J. B. Le Cam, X. Balandraud, E. Toussaint and J. Caillard, *Polymer*., 2013, **54**, 2717-2726.

14. J. R. S. Martinez, J. B. Le Cam, X. Balandraud, E. Toussaint and J. Caillard., *Polymer*., 2013, **54**, 2727-2736.

15. J. C. Mitchell and D. J. Meier, *Journal of Polymer Science Part A-2: Polymer Physics*., 1968, **6**, 1689-1703.

16. Y. Miyamoto, H. Yamao and K. Sekimoto, *Macromolecules.,* 2003, **36**, 6462-6471.

17. M. Tosaka, K. Senoo, K. Sato, M. Noda and N. Ohta, *Polymer.,* 2012, **53**, 864-872.

18. K. Bruning, K. Schneider, S. V. Roth and G. Heinrich, *Macromolecules.,* 2012, **45**, 7914-7919.

19. H. Kawai, *Rheol. Acta.*, 1975, **14**, 27-47.

20. P. A. Albouy, G. Guillier, D. Petermann, A. Vieyres, O. Sanseau and P. Sotta, *Polymer*., 2012, **53**, 3313-3324.

21. N. Candau, L. Chazeau, J. M Chenal, C. Gauthier, J. Ferreira, E. Munch and C. Rochas, *Polymer*., 2012, **53**, 2540-2543.

22. J. Rault, J. Marchal, P. Judeinstein and P. A. Albouy, *Eur. Phys. J. E: Soft Matter Biol. Phys*., 2006, **21**, 243-261.

23. S. Toki, I. Sics, B. S. Hsiao, M. Tosaka, S. Poompradub, Y. Ikeda and S. Kohjiya, *Macromolecules*., 2005, **38**, 7064-7073.

24. Rauline, R. U.S. Pat., 5,227,425, 1993.

25. P. J. Flory and J. Rehner, *Journal of Chemical Physics*., 1943, **11**, 521-526.

26. J. M. Chenal, L. Chazeau, L. Guy, Y. Bomal and C. Gauthier, *Polymer*., 2007, **48**, 1042-1046.

27. P. A. Albouy, J. Marchal and J. Rault, *Eur. Phys. J. E: Soft Matter Biol. Phys*., 2005, **17**, 247-259.

28. G. R. Mitchell, *Polymer.*, 1984, **25**, 1562-1572.

29. S. Trabelsi, S, Ph.D. Thesis, Université d’Orsay, Paris 11, 2002.

30. N. Candau, R. Laghmach, L. Chazeau, J. M. Chenal, C. Gauthier, T. Biben and E. Munch, *Macromolecules.*, 2014, **47**, 5815-5824.

31 N. Candau, R. Laghmach, L. Chazeau, J. M. Chenal, C. Gauthier, T. Biben and E. Munch, *European Polymer Journal.*, 2015, **64**, 244-252.

32 N. Candau, L. Chazeau, J. M. Chenal, C. Gauthier and E. Munch, *Composites Science and Technology*., 2015, **108**, 9-15.

33 M. Tosaka, S. Murakami, S. Poompradub, S. Kohjiya, Y. Ikeda, S. Toki, I. Sics and B. S. Hsiao, *Macromolecules.,* 2004, **37**, 3299-3309.

34 S. Trabelsi, P. A. Albouy and J. Rault, *Macromolecules*., 2003, **36**, 7624-7639.

35 N. Candau, R. Laghmach, L. Chazeau, J. M. Chenal, C. Gauthier, T. Biben and E. Munch, *Polymer.*, 2015, **60**, 115-124.

36 J. D. Hoffman, *J. Res. Nat. Bur. Std.*, 1979, **84**, 359-384.

37 R. Laghmach, T. Biben, L. Chazeau and J.M Chenal, *Constitutive Models for Rubber VIII*, 2013, 473.